

Title:

Single-shot autofocusing of microscopy images using deep learning

Authors:

Yilin Luo^{1,2,3,†}, Luzhe Huang^{1,2,3,†}, Yair Rivenson^{1,2,3,*}, Aydogan Ozcan^{1,2,3,4,*}

Affiliations:

¹Electrical and Computer Engineering Department, University of California, Los Angeles, California 90095, USA

²Bioengineering Department, University of California, Los Angeles, California 90095, USA

³California Nano Systems Institute (CNSI), University of California, Los Angeles, California 90095, USA

⁴David Geffen School of Medicine, University of California Los Angeles, California 90095, USA

[†]Equal contribution authors

^{*}Correspondence: Drs. Aydogan Ozcan and Yair Rivenson

E-mail: ozcan@ucla.edu ; rivensonyair@ucla.edu

Abstract

Autofocusing is a critical step for high-quality microscopic imaging of specimens, especially for measurements that extend over time covering large fields-of-view. Autofocusing is generally practiced using two main approaches. Hardware-based optical autofocusing methods rely on additional distance sensors that are integrated with a microscopy system. Algorithmic autofocusing methods, on the other hand, regularly require axial scanning through the sample volume, leading to longer imaging times, which might also introduce phototoxicity and photobleaching on the sample. Here, we demonstrate a deep learning-based *offline* autofocusing method, termed Deep-R, that is trained to rapidly and blindly autofocus a single-shot microscopy image of a specimen that is acquired at an arbitrary out-of-focus plane. We illustrate the efficacy of Deep-R using various tissue sections that were imaged using fluorescence and brightfield microscopy modalities and demonstrate snapshot autofocusing under different scenarios, such as a uniform axial defocus as well as a sample tilt within the field-of-view. Our results reveal that Deep-R is significantly faster when compared with standard online algorithmic autofocusing methods. This deep learning-based blind autofocusing framework opens up new opportunities for rapid microscopic imaging of large sample areas, also reducing the photon dose on the sample.

Introduction

A critical step in microscopic imaging over an extended spatial or temporal scale is focusing. For example, during longitudinal imaging experiments, focus drifts can occur as a result of mechanical or thermal fluctuations of the microscope body¹ or microscopic specimen movement when for example live cells or model organisms are imaged. Another frequently encountered scenario which also requires autofocusing is due to the nonuniformity of the specimen's topography². Manual focusing is impractical, especially for microscopic imaging over an extended period of time or a large specimen area.

Conventionally, microscopic autofocusing is performed “online”, where the focus plane of each individual field-of-view (FOV) is found during the image acquisition process. Online autofocusing can be generally categorized into two groups: optical³⁻⁹ and algorithmic methods¹⁰⁻¹³. Optical methods typically adopt additional distance sensors involving e.g., a near-infrared laser³⁻⁵, a light-emitting diode⁶ or an additional camera^{7-9,14}, that measure or calculate the relative sample distance needed for the correct focus. These optical methods require modifications to the optical imaging system, which are not always compatible with the existing microscope hardware¹⁵. Algorithmic methods, on the other hand, extract an image sharpness function/measure at different axial depths and locate the best focal plane using an iterative search algorithm. However, the focus function is in general sensitive to the image intensity and contrast, which in some cases can be trapped in a false local maxima/minima¹⁶. Another limitation of these algorithmic autofocusing methods is the requirement to capture *multiple* images through an axial scan (search) within the specimen volume. This process is naturally time-consuming, does not support high frame-rate imaging of dynamic specimen and increases the probability of sample photobleaching, photodamage or phototoxicity¹⁷. As an alternative, wavefront sensing-based autofocusing techniques¹⁸⁻²⁰ also lie at the intersection of optical and algorithmic methods. However, multiple image capture is still required, and therefore these methods also suffer from similar problems as the other algorithmic autofocusing methods face.

In recent years, deep learning has been demonstrated as a powerful tool in solving various inverse problems in microscopic imaging²¹, for example, cross-modality super-resolution^{22,23}, virtual staining^{24,25}, localization microscopy^{26,27}, phase recovery and holographic image reconstruction^{28–30}. Unlike most inverse problem solutions that require a carefully formulated forward model, deep learning instead uses image data to indirectly derive the relationship between the input and the target output distributions. Once trained, the neural network takes in a new sample's image (input) and rapidly reconstructs the desired output without any iterations, parameter tuning or user intervention.

Motivated by the success of deep learning-based solutions to inverse imaging problems, recent works have also explored the use of deep learning for *online* autofocusing of microscopy images^{15,16,31,32}. Some of these previous approaches combined hardware modifications to the microscope design with a neural network; for example, Pinkard *et al.* designed a fully connected Fourier neural network (FCFNN) that utilized additional off-axis illumination sources to predict the axial focus distance from a single image³¹. As another example, Jiang *et al.* treated autofocusing as a regression task and employed a convolutional neural network (CNN) to estimate the focus distance without any axial scanning¹⁵. Dastidar *et al.* improved upon this idea and proposed to use the difference of two defocused images as input to the neural network, which showed higher focusing accuracy¹⁶. However, in the case of an uneven or tilted specimen in the FOV, all the techniques described above are unable to bring the whole region into focus simultaneously. Recently, a deep learning based virtual re-focusing method which can handle non-uniform and spatially-varying blurs has also been demonstrated³². By appending a pre-defined digital propagation matrix (DPM) to a blurred input image, a trained neural network can digitally refocus the input image onto a user-defined 3D surface that is mathematically determined by the DPM. This approach, however, does not perform autofocusing of an image as the DPM is user-defined, based on the specific plane or 3D surface that is desired at the network output.

Other post-processing methods have also been demonstrated to restore a sharply focused image from an acquired defocused image. One of the classical approaches that has been frequently used is to treat the

defocused image as a convolution of the defocusing point spread function (PSF) with the in-focus image. Deconvolution techniques such as the Richardson-Lucy^{33,34} algorithm require accurate prior knowledge of the defocusing PSF, which is not always available. Blind deconvolution methods^{35,36} can also be used to restore images through the optimization of an objective function; but these methods are usually computationally costly, sensitive to image signal-to-noise ratio (SNR) and the choice of the hyperparameters used, and are in general not useful if the blur PSF is spatially varying. There are also some emerging methods that adopt deep learning for blind estimation of a space-variant PSF in optical microscopy³⁷.

Here we introduce a deep-learning based *offline* autofocusing method, termed Deep-R (Fig. 1), that enables the blind transformation of a single-shot defocused image into an in-focus image without any prior knowledge of the defocus distance, its direction, or the blur PSF, whether it is spatially-varying or not. Compared to the existing body of autofocusing methods that have been used in optical microscopy, Deep-R is unique in a number of ways: (1) it does not require any hardware modifications to an existing microscope design; (2) it only needs a single image capture to infer and synthesize the in-focus image, enabling higher imaging throughput and reduced photon dose on the sample, without sacrificing the resolution; (3) its autofocusing is based on a data-driven, non-iterative image inference process that does not require any prior knowledge of the forward imaging model or the defocus distance; and (4) it is broadly applicable to blindly autofocus spatially uniform and non-uniform defocused images, computationally extending the depth of field (DOF) of the imaging system.

Deep-R is based on a generative adversarial network (GAN)³⁸ that is trained with accurately paired in-focus and defocused image pairs. After its training, the generator network rapidly transforms a single defocused fluorescence image into an in-focus image. We demonstrated the performance of Deep-R using various fluorescence (including autofluorescence and immunofluorescence) and brightfield microscopy images with spatially uniform as well as non-uniform defocus within the FOV. Our results reveal that

Deep-R significantly enhances the imaging speed of a benchtop microscope by ~15-fold by eliminating the need for axial scanning during the autofocusing process.

This data-driven offline autofocusing approach will be especially useful in high-throughput imaging over large sample areas, where focusing errors inevitably occur, especially over longitudinal imaging experiments. With Deep-R, the DOF of the microscope and the range of usable images can be significantly extended, thus reducing the time, cost and labor required for reimaging of out-of-focus areas of a sample. Simple to implement and purely computational, Deep-R can be applicable to a wide range of microscopic imaging modalities, as it requires no hardware modifications to the imaging system.

Results

Deep-R based autofocusing of defocused fluorescence images

Fig. 2(a) demonstrates Deep-R based autofocusing of a single defocused immunofluorescence image of an ovarian tissue section. In the training stage, the network was fed with accurately paired/registered image data composed of (1) fluorescence images acquired at different axial defocus distances, and (2) the corresponding in-focus images (ground-truth labels), which were algorithmically calculated using an axial image stack ($N = 101$ images captured at different planes; see the Methods section). During the inference process, a pretrained Deep-R network blindly takes in a single defocused image at an arbitrary defocus distance (within the axial range included in the training), and digitally autofocuses it to match the ground truth image. Fig. 2(b) highlights a sample region of interest (ROI) to illustrate the blind output of Deep-R at different input defocus depths. Within the $\pm 5 \mu\text{m}$ axial training range, Deep-R successfully autofocuses the input images and brings back sharp structural details, e.g., corresponding to SSIM (structural similarity index) values above 0.7, whereas the mechanically scanned input images degrade rapidly, as expected, when the defocus distance exceeds $\sim 0.65 \mu\text{m}$, which corresponds to the DOF of the

objective lens (40×/0.95NA). Even beyond its axial training range, Deep-R output images still exhibit some refocused features, as illustrated in Fig. 2b.

Similar blind inference results were also obtained for a densely-connected human breast tissue sample (see Fig. 3) that is imaged under a 20×/0.75NA objective lens, where Deep-R accurately autofocused the autofluorescence images of the sample within an axial defocus range of $\pm 5 \mu\text{m}$.

Deep-R based autofocusing of non-uniformly defocused images

Although Deep-R is trained on *uniformly* defocused microscopy images, during blind testing it can also successfully autofocus *non-uniformly* defocused images without any prior knowledge of the image distortion or defocusing. As an example, Fig. 4 illustrates Deep-R based autofocusing of a non-uniformly defocused image of a human breast tissue sample that had $\sim 1.5^\circ$ planar tilt (corresponding to an axial difference of $\delta z = 4.356 \mu\text{m}$ within the effective FOV of a 20×/0.75NA objective lens). This Deep-R network was trained using only uniformly defocused images and is the same network that generated the results reported in Fig.3. As illustrated in Fig. 4, at different focal depths (e.g., $z = 0 \mu\text{m}$ and $z = -2.2 \mu\text{m}$), because of the sample tilt, different sub-regions within the FOV were defocused by different amounts, but they were simultaneously autofocused by Deep-R, all in parallel, generating an extended DOF image that matches the reference image (Fig. 4(b), see the Methods section). Moreover, we quantified the focusing performance of Deep-R on this tilted sample using a row-based sharpness coefficient (Fig. 4c, see the Methods section), which reports, row by row, the relative sharpness of the output (or the input) images with respect to the reference image along the direction of the sample tilt (i.e., y-axis). As demonstrated in Fig. 4(c), Deep-R output images achieved a significant increase in sharpness measure within the entire FOV, validating Deep-R's autofocusing capability for a non-uniformly defocused, tilted sample. Fig. 4(c) was calculated on a single sample FOV; Supplementary Fig. 1 reports the statistical analysis of Deep-R results on the whole image dataset consisting of 18 FOVs that are each non-uniformly defocused, confirming the same conclusion as in Fig. 4c.

Point spread function analysis of Deep-R performance

To further quantify the autofocusing capability of Deep-R, we imaged samples containing 300 nm polystyrene beads (excitation and emission wavelengths of 538 nm and 584 nm, respectively) using a 40×/0.95NA objective lens and trained two different neural networks with an axial defocus range of $\pm 5 \mu\text{m}$ and $\pm 8 \mu\text{m}$, respectively. After the training phase, we then measured the 3D PSF of the input image stack and the corresponding Deep-R output image stack by tracking 164 isolated nanobeads across the sample FOV as a function of the defocus distance. For example, Fig. 5(a) illustrates the 3D PSF corresponding to a single nanobead, measured through this axial image stack (input images). As expected, this input 3D PSF shows increased spreading away from the focal plane. On the other hand, the Deep-R PSF corresponding to the output image stack of the same particle maintains a tighter focus, covering an extended depth, determined by the axial training range of the Deep-R network (see Fig. 5a). As an example, at $z = -7 \mu\text{m}$, the output images of a Deep-R network that is trained with $\pm 5 \mu\text{m}$ defocus range exhibit slight defocusing (see Fig. 5b), as expected. However, using a Deep-R network trained with $\pm 8 \mu\text{m}$ defocus range results in accurate refocusing for the same input images (Fig. 5b). Similar conclusions were observed for the blind testing of a 3D sample, where the nanobeads were dispersed within a volume spanning $\sim 20 \mu\text{m}$ thickness (see Supplementary Fig. 2).

Fig. 5(b) further presents the mean and standard deviation of the lateral full width at half maximum (FWHM) values as a function of the axial defocus distance, calculated from 164 individual nanobeads. The enhanced DOF of Deep-R output is clearly illustrated in the nearly constant lateral FWHM within the training range. On the other hand, the mechanically scanned input images show much shallower DOF, as reflected by the rapid change in the lateral FWHM as the defocus distance varies. Note also that the FWHM curve for the input image is unstable at the positive defocus distances, which is caused by the strong side lobes induced by out-of-focus lens aberrations. Deep-R output images, on the other hand, are immune to these defocusing introduced aberrations since it blindly autofocuses the image

at its output and therefore maintains a sharp PSF across the entire axial defocus range that lies within its training, as demonstrated in Fig. 5b.

Comparison of Deep-R computation time against online algorithmic autofocusing methods

While the conventional online algorithmic autofocusing methods require multiple image capture at different depths for each FOV to be autofocused, Deep-R instead reconstructs the in-focus image from a single shot at an arbitrary depth (within its axial training range). This unique feature greatly reduces the scanning time, which is usually prolonged by cycles of image capture and axial stage movement during the focus search before an in-focus image of a given FOV can be captured. To demonstrate this and emphasize the advantages of Deep-R, we experimentally measured the autofocusing time of 4 commonly used online focusing methods: Vollath-4 (VOL4)³⁹, Vollath-5 (VOL5)³⁹, standard deviation (STD) and normalized variance (NVAR)¹⁰. Table 1 summarizes our results, where we report the autofocusing time per 1mm² of sample FOV. Overall, these online algorithms take ~40 s/mm² to autofocus an image using a 3.5 GHz Intel Xeon E5-1650 CPU, while Deep-R inference takes ~ 20 s/mm² on the same CPU, and ~3 s/mm² on an Nvidia GeForce RTX 2080Ti GPU.

Comparison of Deep-R autofocusing quality with offline deconvolution techniques

Next, we compared Deep-R autofocusing against standard deconvolution techniques, specifically, the Landweber deconvolution⁴⁰ and the Richardson-Lucy (RL) deconvolution^{33,34}, using the ImageJ plugin DeconvolutionLab2⁴¹ (see Fig. 6). For these offline deconvolution techniques, the lateral PSFs at the corresponding defocus distances were specifically provided using measurement data, since this information is required for both algorithms to approximate the forward imaging model. In addition to this a priori PSF information at different defocusing distances, the parameters of each algorithm were adjusted/optimized such that the reconstruction had the best visual quality for a fair comparison (see the Methods section). Figure 6 illustrates that at negative defocus distances (e.g., $z = -3 \mu\text{m}$), these offline

deconvolution algorithms demonstrate an acceptable image quality in most regions of the sample, which is expected, as the input image maintains most of the original features at this defocus direction; however, compared with Deep-R output, the Landweber and RL deconvolution results showed inferior performance (despite using the PSF at each defocus distance as *a priori* information). A more substantial difference between Deep-R output and these offline deconvolution methods is observed when the input image is positively defocused (see e.g., $z = 4 \mu\text{m}$ in Fig. 6). Deep-R performs much more improved autofocusing without the need for any PSF information or parameter tuning, which is also confirmed by the SSIM and RMSE (root mean square error) metrics reported in Fig.6.

Deep-R based autofocusing of brightfield microscopy images

While all the previous results are based on images obtained by fluorescence microscopy, Deep-R can also be applied to other incoherent imaging modalities, such as brightfield microscopy. As an example, we applied the Deep-R framework on brightfield microscopy images of an H&E (hematoxylin and eosin) stained human prostate tissue (Fig.7). The training data were composed of images with an axial defocus range of $\pm 10 \mu\text{m}$, which were captured by a $20\times/0.75\text{NA}$ objective lens. After the training phase, the Deep-R network, as before, takes in an image at an arbitrary (and unknown) defocus distance and blindly outputs an in-focus image that matches the ground truth. Although the training images were acquired from a non-lesion prostate tissue sample, blind testing images were obtained from a different sample slide *with* tumor, still achieving high RMSE and SSIM accuracy at the network output (see Fig.7 and Supplementary Fig.3), which indicates the generalization success of our presented method. The application of Deep-R to brightfield microscopy can significantly accelerate whole slide imaging (WSI) systems used in pathology by capturing only a single image at each scanning position within a large sample FOV, thus enabling high-throughput histology imaging.

Discussion

We presented a deep learning-based autofocusing framework, termed Deep-R, that enables offline,

blind autofocusing from a single microscopy image. Although trained with uniformly defocused images, Deep-R can successfully autofocus images of samples that have non-uniform aberrations, computationally extending the DOF of the microscopic imaging system. Stated differently, Deep-R is a data-driven, blind autofocusing algorithm that works without any prior knowledge regarding the defocus distance or aberrations in the optical imaging system. This deep learning-based framework has the potential to transform experimentally acquired images that were deemed unusable due to e.g., out-of-focus sample features, into in-focus images, significantly saving imaging time, cost and labor that would normally be needed for re-imaging of such out-of-focus regions of the sample.

In addition to post-correction of out-of-focus or aberrated images, Deep-R also provides a better alternative to existing online focusing methods, achieving higher imaging speed. Software-based conventional online autofocusing methods acquire *multiple* images at each FOV. The microscope captures the first image at an initial position, calculates an image sharpness feature, and moves to the next axial position based on a focus search algorithm. This iteration continues until the image satisfies a sharpness metric. As a result, the focusing time is prolonged, which leads to increased photon flux on the sample, potentially introducing photobleaching, phototoxicity or photodamage. This iterative autofocusing routine also compromises the effective frame rate of the imaging system, which limits the observable features in a dynamic specimen. In contrast, Deep-R performs autofocusing with a single-shot image, without the need for additional image exposures or sample stage movements, retaining the maximum frame rate of the imaging system.

Although the blind autofocusing range of Deep-R can be increased by incorporating images that cover a larger defocusing range, there is a tradeoff between the inference image quality and the axial autofocusing range. To illustrate this tradeoff, we trained 3 different Deep-R networks on the same immunofluorescence image dataset as in Fig. 2, each with a different axial defocus training range, i.e., $\pm 2\mu\text{m}$, $\pm 5\mu\text{m}$, and $\pm 10\mu\text{m}$, respectively. Fig. 8 reports the average and the standard deviation of RMSE and SSIM values of Deep-R input and output images, calculated from a blind testing dataset consisting of

26 FOVs, each with 512×512 pixels. As the axial training range increases, Deep-R accordingly extends its autofocusing range, as shown in Fig. 8. However, a Deep-R network trained with a large defocus distance (e.g., $\pm 10\mu\text{m}$) partially compromises the autofocusing results corresponding to a slightly defocused image (see e.g., the defocus distances 2-5 μm reported in Fig. 8). Stated differently the blind autofocusing task for the network becomes more complicated when the axial training range increases, yielding a sub-optimal convergence for Deep-R (also see Supplementary Fig.4). A possible explanation for this behavior is that as the defocusing range increases, each pixel in the defocused image is receiving contributions from an increasing number of neighboring object features, which renders the inverse problem of remapping these features back to their original locations more challenging. Therefore, the inference quality and the success of autofocusing is empirically related to the sample density as well as the SNR of the acquired raw image.

In comparison to our earlier work, Deep-Z³², which requires a user-defined DPM for refocusing of a fluorescence image to a desired surface, Deep-R achieves *blind* autofocusing using a single acquired image without any prior knowledge of the defocus amount, direction, or the aberration pattern. Stated differently, Deep-Z can be analogous to the focusing knob of a microscope that is digitally operated by a user, and Deep-R is the blind autofocusing unit that automatically finds the best focused image in one shot without any user interventions or *a priori* information.

In conclusion, Deep-R provides a powerful post-imaging, offline autofocusing tool enabled by deep learning. This method is widely applicable to various incoherent imaging modalities e.g., fluorescence microscopy, brightfield microscopy and darkfield microscopy, where the inverse autofocusing solution can be efficiently learned by a deep neural network through image data. This approach significantly increases the overall imaging speed, and would especially be important for high-throughput imaging of large sample areas over extended periods of time, making it feasible to use out-of-focus images without the need for re-imaging the sample, also reducing the overall photon dose on the sample.

Materials and Methods

Sample preparation

Breast, ovarian and prostate tissue samples: the samples were obtained from the Translational Pathology Core Laboratory (TPCL) and prepared by the Histology Lab at UCLA. All the samples were obtained after the de-identification of the patient related information and prepared from existing specimens. Therefore, this work did not interfere with standard practices of care or sample collection procedures. The human tissue blocks were sectioned using a microtome into 4 μm thick sections, followed by deparaffinization using Xylene and mounting on a standard glass slide using CytosealTM (Thermo-Fisher Scientific, Waltham, MA, USA). The ovarian tissue slides were labelled by pan-cytokeratin tagged by fluorophore Opal 690, and the prostate tissue slides were stained with H&E.

Nano-bead sample preparation: 300 nm fluorescence polystyrene latex beads (with excitation/emission at 538/584nm) were purchased from MagSphere (PSFR300NM), diluted 3,000 \times using methanol. The solution is ultrasonicated for 20 min before and after dilution to break down clusters. 2.5 μL of diluted bead solution was pipetted onto a thoroughly cleaned #1 coverslip and let dry.

3D nanobead sample preparation: following a similar procedure as described above, nanobeads were diluted 3,000 \times using methanol. 10 μL of Prolong Gold Antifade reagent with DAPI (ThermoFisher P-36931) was pipetted onto a thoroughly cleaned glass slide. A droplet of 2.5 μL of diluted bead solution was added to Prolong Gold reagent and mixed thoroughly. Finally, a cleaned coverslip was applied to the slide and let dry.

Image acquisition

The autofluorescence images of breast tissue sections were obtained by an inverted microscope (IX83, Olympus), controlled by the Micro-Manager microscope automation software. The unstained tissue was excited near the ultraviolet range and imaged using a DAPI filter cube (OSF13-DAPI-5060C, EX377/50, EM447/60, DM409, Semrock). The images were acquired with a 20 \times /0.75NA objective lens (Olympus UPLSAPO 20 \times /0.75NA, WD 0.65). At each FOV of the sample, autofocusing was algorithmically

performed, and the resulting plane was set as the initial position (i.e., reference point), $z = 0 \mu\text{m}$. The autofocus was controlled by the OughtaFocus plugin⁴² in Micro-Manager⁴³, which uses Brent's algorithm⁴⁴ for searching of the optimal focus based on Vollath-5³⁹ criterion. For the training and validation datasets, the z-stack was taken from $-10 \mu\text{m}$ to $10 \mu\text{m}$ with $0.5 \mu\text{m}$ axial spacing (DOF = $0.8 \mu\text{m}$). For the testing image dataset, the axial spacing was $0.2 \mu\text{m}$. Each image was captured with a scientific CMOS image sensor (ORCA-flash4.0 v.2, Hamamatsu Photonics) with an exposure time of $\sim 100 \text{ ms}$.

The immunofluorescence images of human ovarian samples were imaged on the same platform with a $40\times/0.95\text{NA}$ objective lens (Olympus UPLSAPO $40\times/0.95\text{NA}$, WD 0.18), using a Cy5 filter cube (CY5-4040C-OFX, EX628/40, EM692/40, DM660, Semrock). After performing the autofocus, a z-stack was obtained from $-10 \mu\text{m}$ to $10 \mu\text{m}$ with $0.2 \mu\text{m}$ axial steps.

Similarly, the nanobeads sample were imaged with the same $40\times/0.95\text{NA}$ objective lens, using a Texas red filter cube (OSFI3-TXRED-4040C, EX562/40, EM624/40, DM593, Semrock), and a z-stack was obtained from $-10 \mu\text{m}$ to $10 \mu\text{m}$ with $0.2 \mu\text{m}$ axial steps after the autofocus step ($z = 0 \mu\text{m}$).

Finally, the H&E stained prostate samples were imaged on the same platform using brightfield mode with a $20\times/0.75\text{NA}$ objective lens (Olympus UPLSAPO $20\times/0.75\text{NA}$, WD 0.65). After performing autofocus on the automation software, a z-stack was obtained from $-10 \mu\text{m}$ to $10 \mu\text{m}$ with an axial step size of $0.5 \mu\text{m}$.

Data pre-processing

To correct for rigid shifts and rotations resulting from the microscope stage, the image stacks were first aligned using the ImageJ plugin 'StackReg'⁴⁵. Then, an extended DOF (EDOF) image was generated using the ImageJ plugin 'Extended Depth of Field'⁴⁶ for each FOV, which typically took $\sim 180 \text{ s/FOV}$ on a computer with i9-7900X CPU and 64GB RAM. The stacks and the corresponding EDOF images were cropped into non-overlapping 512×512 -pixel image patches in the lateral direction, and the *ground truth* image was set to be the one with the highest SSIM with respect to the EDOF image. Then, a series of defocused planes, above and below the focused plane, were selected as input images and input-label image

pairs were generated for network training. The image datasets were randomly divided into training and validation datasets with a preset ratio of 0.85:0.15 with *no overlap* in FOV. Note also that the blind testing dataset was cropped from separate FOVs from *different* sample slides that did *not* appear in the training and validation datasets. Training images are augmented 8 times by random flipping and rotations during the training, while the validation dataset was not augmented. Each pair of input and ground truth images were normalized such that they have zero mean and unit variance before they were fed into the corresponding Deep-R network. The total number of FOVs, as well as the number of defocused images at each FOV used for training, validation and blind testing of the networks are summarized in Supplementary Table 1.

Network structure, training and validation

A GAN is used to perform snapshot autofocusing (see Supplementary Fig. 5). The GAN consists of a generator network and a discriminator network. The generator network follows a U-net⁴⁷ structure with residual connections, and the discriminator network is a convolutional neural network, following a structure demonstrated in previous papers^{24,32}. During the training phase, the network iteratively minimizes the loss functions of the generator and discriminator networks, defined as:

$$L_G = \lambda \times (1 - D(G(x)))^2 + \nu \times \text{MSSSIM}(y, G(x)) + \xi \times \text{BerHu}(y, G(x)) \quad (1)$$

$$L_D = D(G(x))^2 + (1 - D(y))^2 \quad (2)$$

where x represents the defocused input image, y denotes the in-focus image used as ground truth, $G(x)$ denotes the generator output, $D(\cdot)$ is the discriminator inference. The generator loss function (L_G) is a combination the adversarial loss with two additional regularization terms: the multiscale structural similarity (MSSSIM) index⁴⁸ and the reversed Huber loss (BerHu)^{49,50}, balanced by regularization parameters λ, ν, ξ . In our training, these parameters are set empirically such that three sub-types of losses contributed approximately equally after the convergence. MSSSIM is defined as:

$$\text{MSSSIM}(x, y) = \left[\frac{2\mu_{x_M}\mu_{y_M} + C_1}{\mu_{x_M}^2 + \mu_{y_M}^2 + C_1} \right]^{\alpha_M} \cdot \prod_{j=1}^M \left[\frac{2\sigma_{x_j}\sigma_{y_j} + C_2}{\sigma_{x_j}^2 + \sigma_{y_j}^2 + C_2} \right]^{\beta_j} \left[\frac{\sigma_{x_j y_j} + C_3}{\sigma_{x_j}\sigma_{y_j} + C_3} \right]^{\gamma_j} \quad (3)$$

where x_j and y_j are the distorted and reference images downsampled 2^{j-1} times, respectively; μ_x, μ_y are the averages of x, y ; σ_x^2, σ_y^2 are the variances of x, y ; σ_{xy} is the covariance of x, y ; C_1, C_2, C_3 are constants used to stabilize the division with a small denominator; and $\alpha_M, \beta_j, \gamma_j$ are exponents used to adjust the relative importance of different components. The MSSSIM function is implemented using the Tensorflow⁵¹ function `tf.image.ssim_multiscale`, using its default parameter settings. The BerHu loss is defined as:

$$\text{BerHu}(x, y) = \sum_{\substack{m,n \\ |x(m,n)-y(m,n)| \leq c}} |x(m, n) - y(m, n)| + \sum_{\substack{m,n \\ |x(m,n)-y(m,n)| > c}} \frac{[x(m, n) - y(m, n)]^2 + c^2}{2c} \quad (4)$$

where $x(m, n)$ refers to the pixel intensity at point (m, n) of an image of size $M \times N$, c is a hyperparameter, empirically set as $\sim 10\%$ of the standard deviation of the normalized ground truth image.

All the weights of the convolutional layers were initialized using a truncated normal distribution (Glorot initializer), while the weights for the fully connected (FC) layers were initialized to 0.1. An adaptive moment estimation (Adam)⁴² optimizer was used to update the learnable parameters, with a learning rate of 5×10^{-4} for the generator and 1×10^{-6} for the discriminator, respectively. In addition, six updates of the generator loss and three updates of the discriminator loss are performed at each iteration. We used a batch size of 5 in our training phase, and the validation set was tested every 50 iterations. The training process converges after $\sim 100,000$ iterations (equivalent to ~ 50 epochs) and the best model is chosen as the one with the smallest BerHu loss on the validation set, which was empirically found to perform better.

Implementation details

The network is implemented using TensorFlow on a PC with Intel Xeon Core W-2195 CPU at 2.3GHz and 256 GB RAM, using Nvidia GeForce RTX 2080Ti GPU. The training phase using $\sim 30,000$ image pairs (512 \times 512 pixels in each image) takes about ~ 30 hours. After the training, the blind inference (autofocusing) process on a 512 \times 512-pixel input image takes ~ 0.1 sec.

Image quality analysis

Difference image calculation: the raw inputs and the network outputs were originally 16-bit. For demonstration, we normalized all the inputs, outputs and ground truth images to the same scale. The absolute difference images of the input and output with respect to the ground truth were normalized to another scale such that the maximum error was 255.

Image sharpness coefficient for tilted sample images: Since there was no ground truth for the tilted samples, a reference image was synthesized using a maximum intensity projection (MIP) along the axial direction, incorporating 10 planes between $z = 0 \mu\text{m}$ and $z = 1.8 \mu\text{m}$ for the best visual sharpness. Following this, the input and output images were first convolved with a Sobel operator to calculate a sharpness map, S , defined as:

$$S(I) = \sqrt{I_X^2 + I_Y^2} \quad (5)$$

where I_X, I_Y represent the gradients of the image I along X and Y axis, respectively. The relative sharpness of each row with respect to the reference image was calculated as the ordinary least square (OLS) coefficient without intercept⁵²:

$$\hat{\alpha}_i = \frac{S(x)_i S(y)_i^T}{S(y)_i S(y)_i^T}, i = 1, 2, \dots, N \quad (6)$$

where S_i is the i -th row of S , y is the reference image, N is the total number of rows.

The standard deviation of the relative sharpness is calculated as:

$$\text{Std}(\hat{\alpha}_i) = \sqrt{\frac{\text{RSS}_i}{(N-1) \cdot S(y)_i \cdot S(y)_i^T}}, \quad \text{RSS}_i = \sum (S(x)_i - \hat{\alpha}_i S(y)_i)^2 \quad (7)$$

where RSS_i stands for the sum of squared residuals of OLS regression at the i^{th} row.

Estimation of the lateral FWHM values for PSF analysis

A threshold was applied to the most focused plane (with the largest image standard deviation)

within an acquired axial image stack to extract the connected components. Individual regions of 30×30 pixels were cropped around the centroid of the sub-regions. A 2D Gaussian fit (*lsqcurvefit*) using Matlab (MathWorks) was performed on *each* plane in each of the regions to retrieve the evolution of the lateral FWHM, which was calculated as the mean FWHM of x and y directions. For each of the sub-regions, the fitted centroid at the most focused plane was used to crop a x - z slice, and another 2D Gaussian fit was performed on the slice to estimate the axial FWHM. Using the statistics of the *input* lateral and axial FWHM at the focused plane, a threshold was performed on the sub-regions to exclude any dirt and bead clusters from this PSF analysis.

Implementation of RL and Landweber image deconvolution algorithms

The image deconvolution (which was used to compare the performance of Deep-R) was performed using the ImageJ plugin DeconvolutionLab2⁴¹. We adjusted the parameters for RL and Landweber algorithm such that the reconstructed images had the best visual quality. For Landweber deconvolution, we used 100 iterations with a gradient descent step size of 0.1. For RL deconvolution, the best image was obtained at the 100th iteration. Since the deconvolution results exhibit known boundary artifacts⁵³ at the edges, we cropped 10 pixels at each image edge when calculating the SSIM and RMSE index to provide a fair comparison against Deep-R results.

Speed measurement of online autofocusing algorithms

The autofocusing speed measurement is performed using the same microscope (IX83, Olympus) with a $20 \times / 0.75\text{NA}$ objective lens using nanobead samples. The online algorithmic autofocusing procedure is controlled by the OughtaFocus plugin⁴² in Micro-Manager⁴³, which uses the Brent's algorithm⁴⁴. We choose the following search parameters: SearchRange = 10 μm , tolerance = 0.1 μm , exposure = 100 ms. Then, we compared the autofocusing time of 4 different focusing criteria: Vollath-4

(VOL4)³⁹, Vollath-5 (VOL5)³⁹, standard deviation (STD) and normalized variance (NVAR)¹⁰. These criteria are defined as follows:

$$F_{VOL4} = \sum_{m=1}^{M-1} \sum_{n=1}^N x(m, n)x(m + 1, n) - \sum_{m=1}^{M-2} \sum_{n=1}^N x(m, n)x(m + 2, n) \quad (8)$$

$$F_{VOL5} = \sum_{m=1}^{M-1} \sum_{n=1}^N x(m, n)x(m + 1, n) - MN\mu^2 \quad (9)$$

$$F_{STD} = \sqrt{\frac{1}{MN} \sum_{m=1}^M \sum_{n=1}^N [x(m, n) - \mu]^2} \quad (10)$$

$$F_{NVAR} = \frac{1}{MN\mu} \sum_{m=1}^M \sum_{n=1}^N [x(m, n) - \mu]^2 \quad (11)$$

where μ is the mean intensity defined as:

$$\mu = \sum_{m=1}^M \sum_{n=1}^N x(m, n) \quad (12)$$

The autofocusing time is measured by the controller software, and the exposure time for the final image capture is excluded from this measurement. The measurement is performed on 4 different FOVs, each measured 4 times, with the starting plane randomly initiated from different heights. The final statistical analysis (Table 1) was performed based on these 16 measurements.

Acknowledgements

The Ozcan Lab at UCLA acknowledges the support of Koc Group, NSF and HHMI. The authors also acknowledge Dr. Jianyu Rao of UCLA Department of Pathology for his assistance with some of the tissue samples.

References

1. Kreft, M., Stenovec, M. & Zorec, R. Focus-Drift Correction in Time-Lapse Confocal Imaging. *Ann. N. Y. Acad. Sci.* **1048**, 321–330 (2005).
2. Shen, F., Hodgson, L. & Hahn, K. [32] - Digital Autofocus Methods for Automated Microscopy. in *Methods in Enzymology* (ed. Inglese, J.) vol. 414 620–632 (Academic Press, 2006).
3. Bathe-Peters, M., Annibale, P. & Lohse, M. J. All-optical microscope autofocus based on an electrically tunable lens and a totally internally reflected IR laser. *Opt. Express* **26**, 2359–2368 (2018).
4. Liron, Y., Paran, Y., Zatorsky, N. G., Geiger, B. & Kam, Z. Laser autofocusing system for high-resolution cell biological imaging. *J. Microsc.* **221**, 145–151 (2006).
5. Liu, C.-S. *et al.* Novel fast laser-based auto-focusing microscope. in *2010 IEEE SENSORS* 481–485 (2010). doi:10.1109/ICSENS.2010.5690153.
6. Liao, J. *et al.* Rapid focus map surveying for whole slide imaging with continuous sample motion. *Opt. Lett.* **42**, 3379–3382 (2017).
7. Montalto, M. C., McKay, R. R. & Filkins, R. J. Autofocus methods of whole slide imaging systems and the introduction of a second-generation independent dual sensor scanning method. *J. Pathol. Inform.* **2**, 44 (2011).
8. Guo, K., Liao, J., Bian, Z., Heng, X. & Zheng, G. InstantScope: a low-cost whole slide imaging system with instant focal plane detection. *Biomed. Opt. Express* **6**, 3210–3216 (2015).
9. Silvestri, L. *et al.* RAPID: Real-time image-based autofocus for all wide-field optical microscopy systems. *bioRxiv* 170555 (2017) doi:10.1101/170555.

10. Redondo, R. *et al.* Autofocus evaluation for brightfield microscopy pathology. *J. Biomed. Opt.* **17**, 036008 (2012).
11. Sun, Y., Duthaler, S. & Nelson, B. J. Autofocusing in computer microscopy: Selecting the optimal focus algorithm. *Microsc. Res. Tech.* **65**, 139–149 (2004).
12. Firestone, L., Cook, K., Culp, K., Talsania, N. & Preston, K. Comparison of autofocus methods for automated microscopy. *Cytometry* **12**, 195–206 (1991).
13. Yazdanfar, S. *et al.* Simple and robust image-based autofocusing for digital microscopy. *Opt. Express* **16**, 8670–8677 (2008).
14. Liao, J. *et al.* Single-frame rapid autofocusing for brightfield and fluorescence whole slide imaging. **6**.
15. Jiang, S. *et al.* Transform- and multi-domain deep learning for single-frame rapid autofocusing in whole slide imaging. *Biomed. Opt. Express* **9**, 1601–1612 (2018).
16. Dastidar, T. R. & Ethirajan, R. Whole slide imaging system using deep learning-based automated focusing. *Biomed. Opt. Express* **11**, 480–491 (2020).
17. Bopp, M. A., Jia, Y., Li, L., Cogdell, R. J. & Hochstrasser, R. M. Fluorescence and photobleaching dynamics of single light-harvesting complexes. *Proc. Natl. Acad. Sci.* **94**, 10630–10635 (1997).
18. Xu, J. *et al.* Accelerating wavefront-sensing-based autofocusing using pixel reduction in spatial and frequency domains. *Appl. Opt.* **58**, 3003–3012 (2019).
19. Jiang, Z., Kong, Y., Liu, F., Liu, C. & Wang, S. Graphics processing unit (GPU) aided wavefront-based autofocusing in microscopy. *AIP Adv.* **8**, 105328 (2018).
20. Xu, J. *et al.* Wavefront-sensing-based autofocusing in microscopy. *J. Biomed. Opt.* **22**, 086012 (2017).

21. Belthangady, C. & Royer, L. A. Applications, promises, and pitfalls of deep learning for fluorescence image reconstruction. *Nat. Methods* **1** (2019) doi:10.1038/s41592-019-0458-z.
22. Rivenson, Y. *et al.* Deep learning microscopy. *Optica* **4**, 1437 (2017).
23. Wang, H. *et al.* Deep learning enables cross-modality super-resolution in fluorescence microscopy. *Nat. Methods* **16**, 103–110 (2019).
24. Rivenson, Y. *et al.* Virtual histological staining of unlabelled tissue-autofluorescence images via deep learning. *Nat. Biomed. Eng.* (2019) doi:10.1038/s41551-019-0362-y.
25. Rivenson, Y. *et al.* PhaseStain: the digital staining of label-free quantitative phase microscopy images using deep learning. *Light Sci. Appl.* **8**, 23 (2019).
26. Nehme, E., Weiss, L. E., Michaeli, T. & Shechtman, Y. Deep-STORM: super-resolution single-molecule microscopy by deep learning. *Optica* **5**, 458–464 (2018).
27. Ouyang, W., Aristov, A., Lelek, M., Hao, X. & Zimmer, C. Deep learning massively accelerates super-resolution localization microscopy. *Nat. Biotechnol.* **36**, 460–468 (2018).
28. Rivenson, Y., Zhang, Y., Günaydın, H., Teng, D. & Ozcan, A. Phase recovery and holographic image reconstruction using deep learning in neural networks. *Light Sci. Appl.* **7**, 17141–17141 (2018).
29. Wu, Y. *et al.* Extended depth-of-field in holographic imaging using deep-learning-based autofocusing and phase recovery. *Optica* **5**, 704–710 (2018).
30. Sinha, A., Lee, J., Li, S. & Barbastathis, G. Lensless computational imaging through deep learning. *Optica* **4**, 1117–1125 (2017).
31. Pinkard, H., Phillips, Z., Babakhani, A., Fletcher, D. A. & Waller, L. Deep learning for single-shot autofocus microscopy. *Optica* **6**, 794–797 (2019).

32. Wu, Y. *et al.* Three-dimensional virtual refocusing of fluorescence microscopy images using deep learning. *Nat. Methods* (2019) doi:10.1038/s41592-019-0622-5.
33. Richardson, W. H. Bayesian-Based Iterative Method of Image Restoration*. *J. Opt. Soc. Am.* **62**, 55 (1972).
34. Lucy, L. B. An iterative technique for the rectification of observed distributions. *Astron. J.* **79**, 745 (1974).
35. Kim, B. & Naemura, T. Blind deconvolution of 3D fluorescence microscopy using depth-variant asymmetric PSF. *Microsc. Res. Tech.* **79**, 480–494 (2016).
36. Levin, A., Weiss, Y., Durand, F. & Freeman, W. T. Understanding Blind Deconvolution Algorithms. *IEEE Trans. Pattern Anal. Mach. Intell.* **33**, 2354–2367 (2011).
37. Shajkofci, A. & Liebling, M. Semi-Blind Spatially-Variant Deconvolution in Optical Microscopy with Local Point Spread Function Estimation By Use Of Convolutional Neural Networks. *2018 25th IEEE Int. Conf. Image Process. ICIP* 3818–3822 (2018) doi:10.1109/ICIP.2018.8451736.
38. Goodfellow, I. *et al.* Generative Adversarial Nets. in *Advances in Neural Information Processing Systems 27* (eds. Ghahramani, Z., Welling, M., Cortes, C., Lawrence, N. D. & Weinberger, K. Q.) 2672–2680 (Curran Associates, Inc., 2014).
39. Vollath, D. The influence of the scene parameters and of noise on the behaviour of automatic focusing algorithms. *J. Microsc.* **151**, 133–146 (1988).
40. Landweber, L. An Iteration Formula for Fredholm Integral Equations of the First Kind. *Am. J. Math.* **73**, 615–624 (1951).
41. Sage, D. *et al.* DeconvolutionLab2: An open-source software for deconvolution microscopy. *Methods* **115**, 28–41 (2017).

42. Autofocus manual - Micro-Manager. https://micro-manager.org/wiki/Autofocus_manual.
43. Edelstein, A. D. *et al.* Advanced methods of microscope control using μ Manager software. *J. Biol. Methods* **1**, e10 (2014).
44. Brent, R. P. *Algorithms for Minimization Without Derivatives*. (Courier Corporation, 2013).
45. Thevenaz, P., Ruttimann, U. E. & Unser, M. A pyramid approach to subpixel registration based on intensity. *IEEE Trans. Image Process.* **7**, 27–41 (1998).
46. Forster, B., Van De Ville, D., Berent, J., Sage, D. & Unser, M. Complex wavelets for extended depth-of-field: A new method for the fusion of multichannel microscopy images. *Microsc. Res. Tech.* **65**, 33–42 (2004).
47. Ronneberger, O., Fischer, P. & Brox, T. U-net: Convolutional networks for biomedical image segmentation. in *Lecture Notes in Computer Science (including subseries Lecture Notes in Artificial Intelligence and Lecture Notes in Bioinformatics)* (2015).
doi:10.1007/978-3-319-24574-4_28.
48. Wang, Z., Simoncelli, E. P. & Bovik, A. C. Multiscale structural similarity for image quality assessment. in *The Thrity-Seventh Asilomar Conference on Signals, Systems Computers, 2003* vol. 2 1398-1402 Vol.2 (2003).
49. Owen, A. B. A robust hybrid of lasso and ridge regression. 59–71 (2007)
doi:10.1090/conm/443/08555.
50. Laina, I., Rupprecht, C., Belagiannis, V., Tombari, F. & Navab, N. Deeper depth prediction with fully convolutional residual networks. *Proc. - 2016 4th Int. Conf. 3D Vis. 3DV 2016* 239–248 (2016) doi:10.1109/3DV.2016.32.

51. Coy, H. *et al.* Deep learning and radiomics: the utility of Google TensorFlow™ Inception in classifying clear cell renal cell carcinoma and oncocytoma on multiphasic CT. *Abdom. Radiol.* **44**, 2009–2020 (2019).
52. Othman, S. A. Comparison between Models With and Without Intercept. 10.
53. Renting Liu & Jiaya Jia. Reducing boundary artifacts in image deconvolution. in *2008 15th IEEE International Conference on Image Processing* 505–508 (2008).
doi:10.1109/ICIP.2008.4711802.

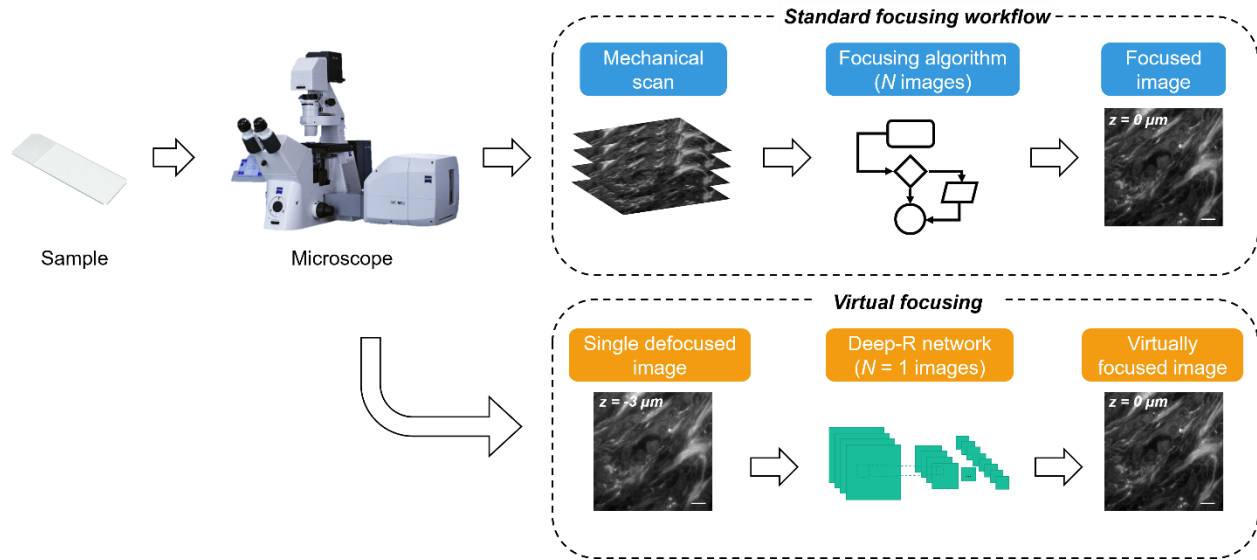


Fig. 1. Deep-R autofocusing. Deep-R blindly autofocuses a defocused image after its capture; mechanical autofocusing methods require multiple image acquisition at different axial locations.

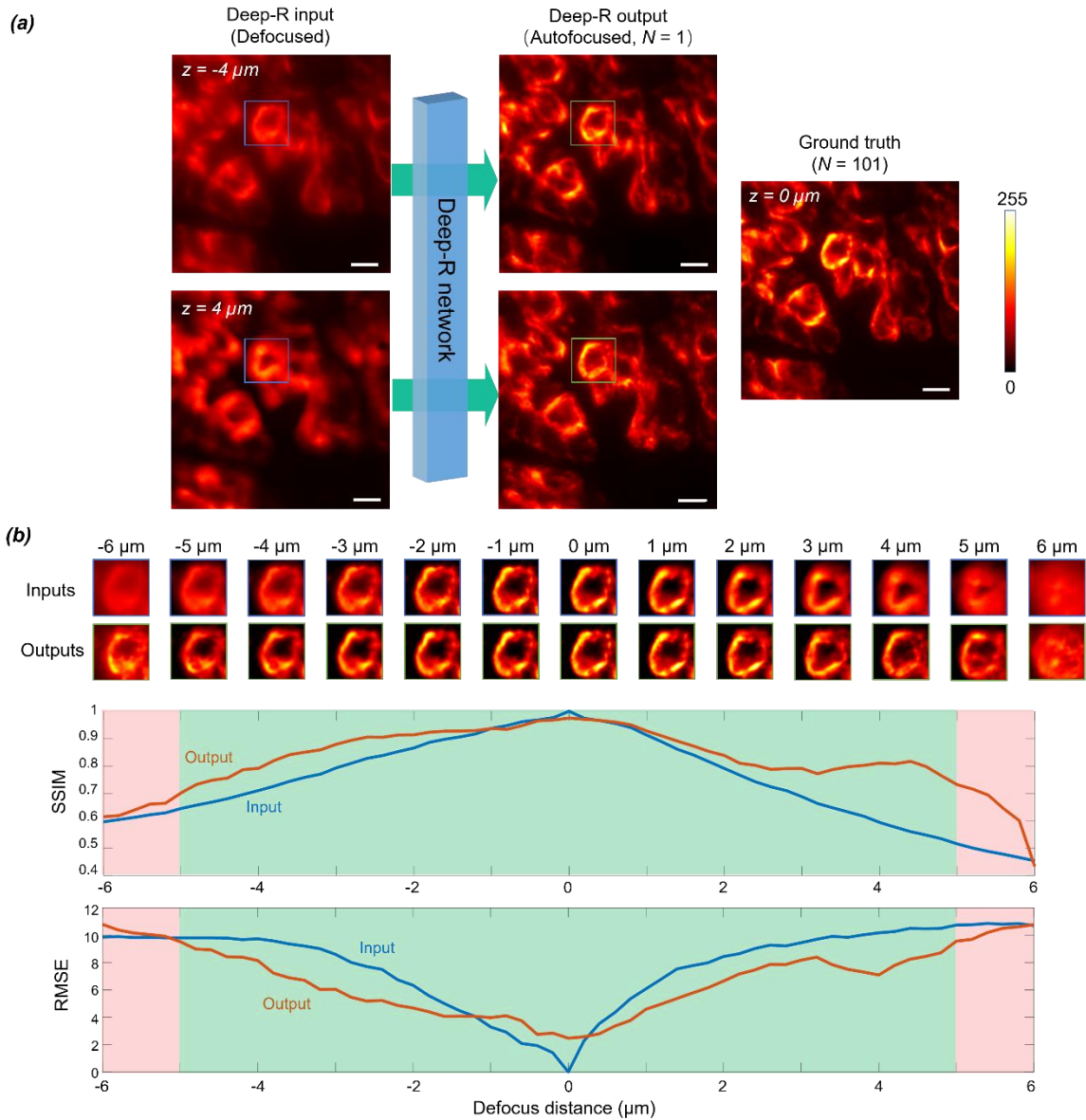


Fig. 2. Deep-R based autofocusing of fluorescently stained samples. (a) Deep-R performs blind autofocusing of individual fluorescence images without prior knowledge of their defocus distances or directions. Scale bars, $10 \mu\text{m}$. (b) For the specific ROI in (a), the SSIM and RMSE values of input and output images with respect to the ground truth ($z = 0 \mu\text{m}$, in-focus image) are plotted as a function of the axial defocus distance. Green zone indicates that the axial defocus distance is within the training range while the red zone indicates that the axial range is outside of the training defocus range.

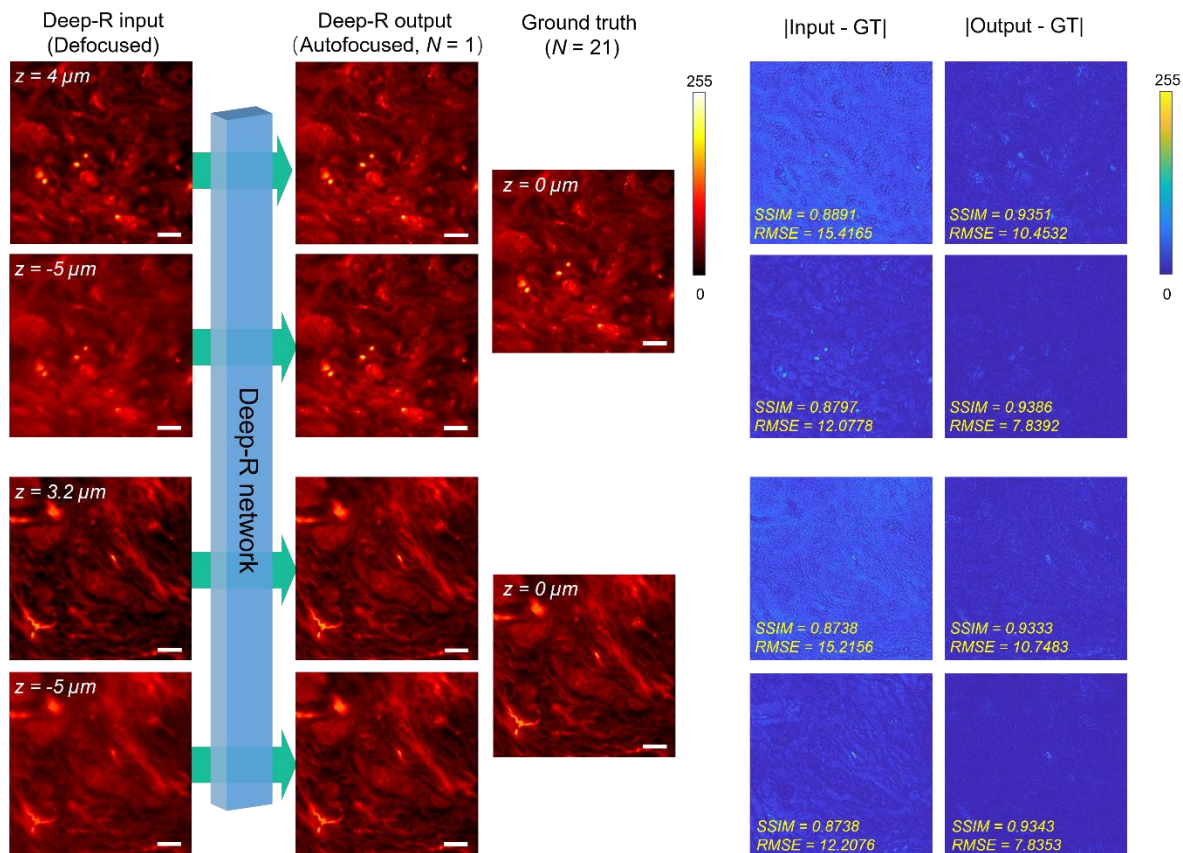


Fig. 3. Deep-R based autofocusing of autofluorescence images. Two different ROIs, each with positive and negative defocus distances, are blindly brought to focus by Deep-R. The absolute difference images of the ground truth with respect to Deep-R input and output images are also shown on the right, with the corresponding SSIM and RMSE quantification reported as insets. Scale bars, 20 μm .

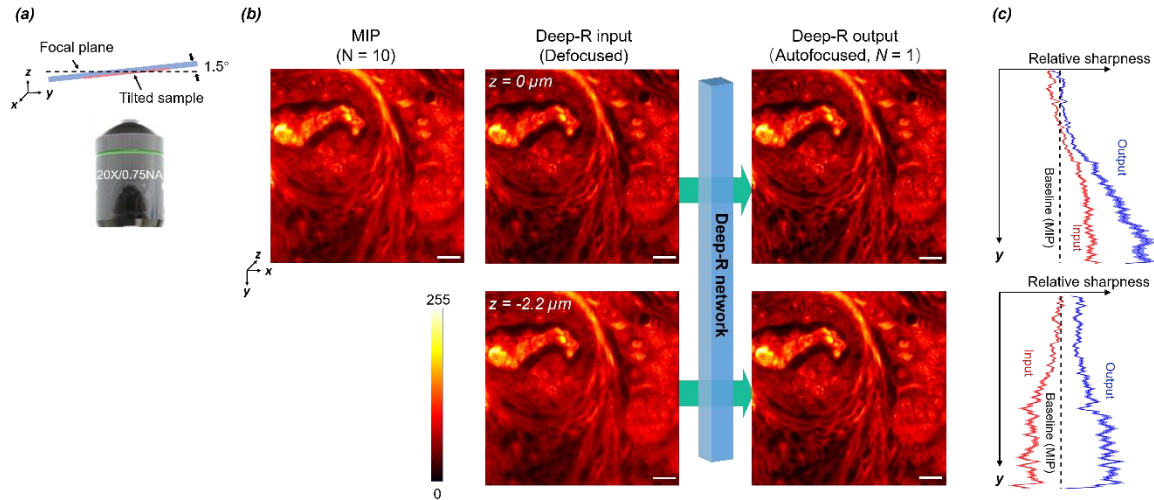


Fig. 4. Deep-R based autofocusing of a non-uniformly defocused fluorescence image. (a) Image acquisition of a tilted autofluorescent sample, corresponding to a depth difference of $\delta z = 4.356 \mu\text{m}$ within the FOV. (b) Deep-R autofocusing results for a tilted sample. Since no real ground truth is available, we used the MIP image, calculated from $N = 10$ images as the reference image in this case. Top row: autofocusing of an input image where the upper region is blurred due to the sample tilt. Second row: autofocusing of an input image where the lower region is blurred due to the sample tilt. Scale bars, $20 \mu\text{m}$. (c) Deep-R output images are quantitatively evaluated using a relative sharpness coefficient that compares the sharpness of each row with the baseline (MIP) image as well as the input image.

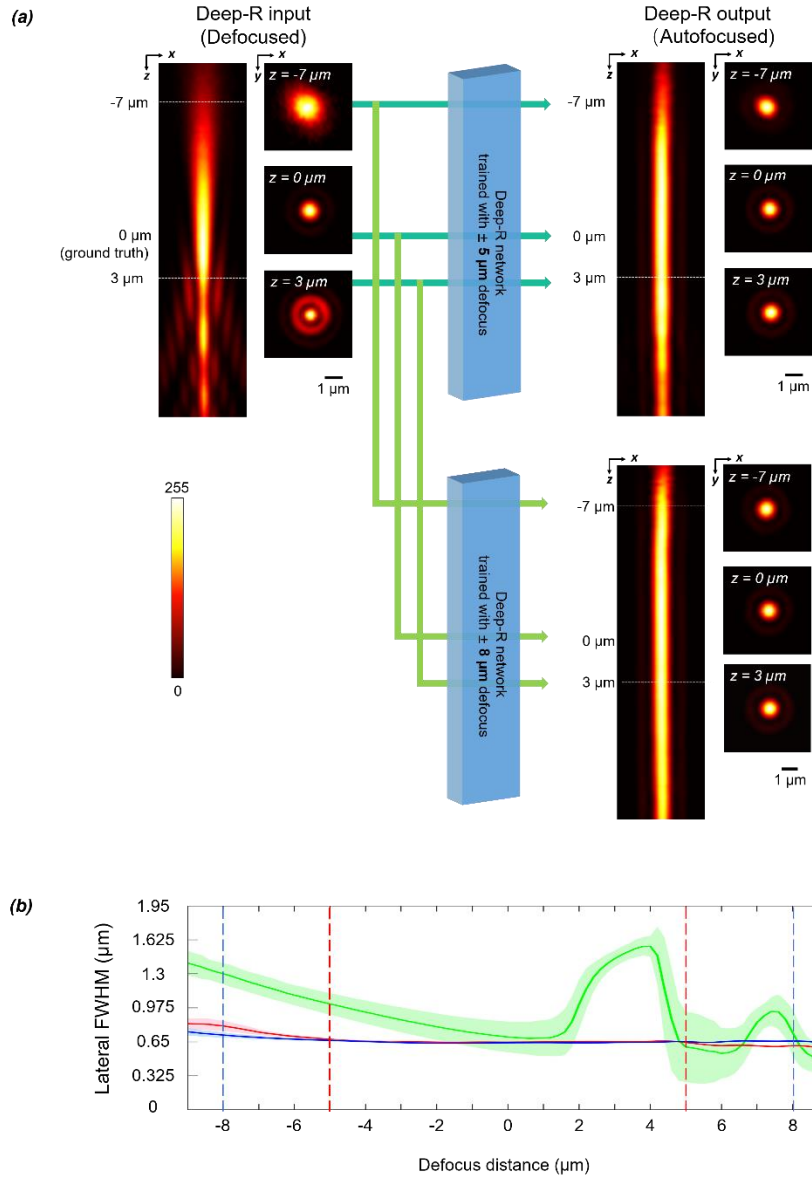


Fig. 5. 3D PSF analysis of Deep-R using 300 nm fluorescent beads. (a) Each plane in the input image stack is fed into Deep-R network and blindly autofocused. (b) Mean and standard deviations of the lateral FWHM values of the particle images are reported as a function of the axial defocus distance. The statistics are calculated from $N = 164$ individual nanobeads. Green curve: FWHM statistics of the mechanically scanned image stack (i.e., the network input). Red curve: FWHM statistics of the output images calculated using a Deep-R network that is trained with $\pm 5 \mu\text{m}$ axial defocus range. Blue curve: FWHM statistics of the output images calculated using a Deep-R network that is trained with $\pm 8 \mu\text{m}$ axial defocus range.

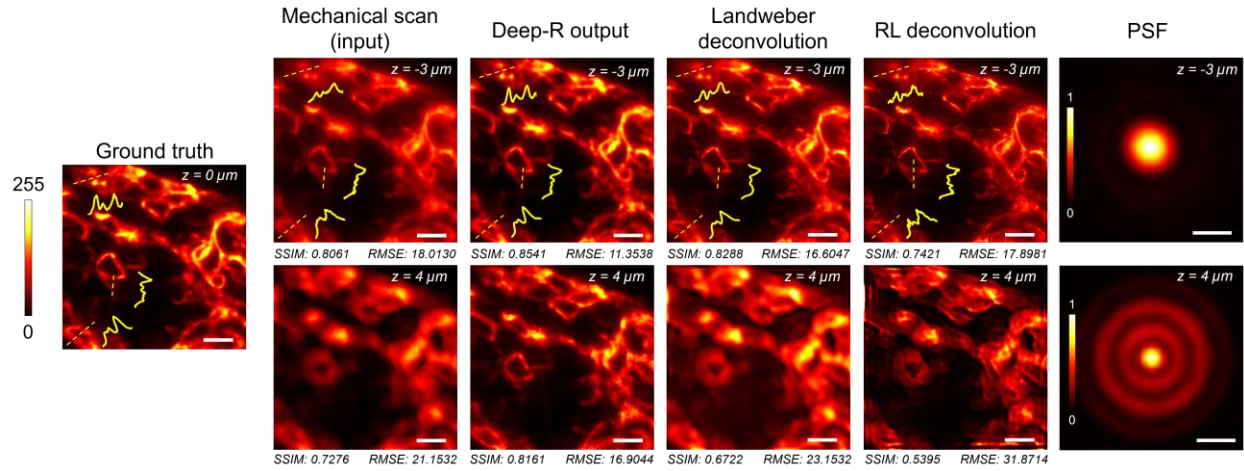


Fig. 6. Comparison of Deep-R autofocusing with deconvolution techniques^{33,34,40}. The lateral PSFs at the corresponding defocus distances are provided to the deconvolution algorithms as prior knowledge of the defocus model. Scale bars for tissue images, 10 μm . Scale bars for PSF images, 1 μm .

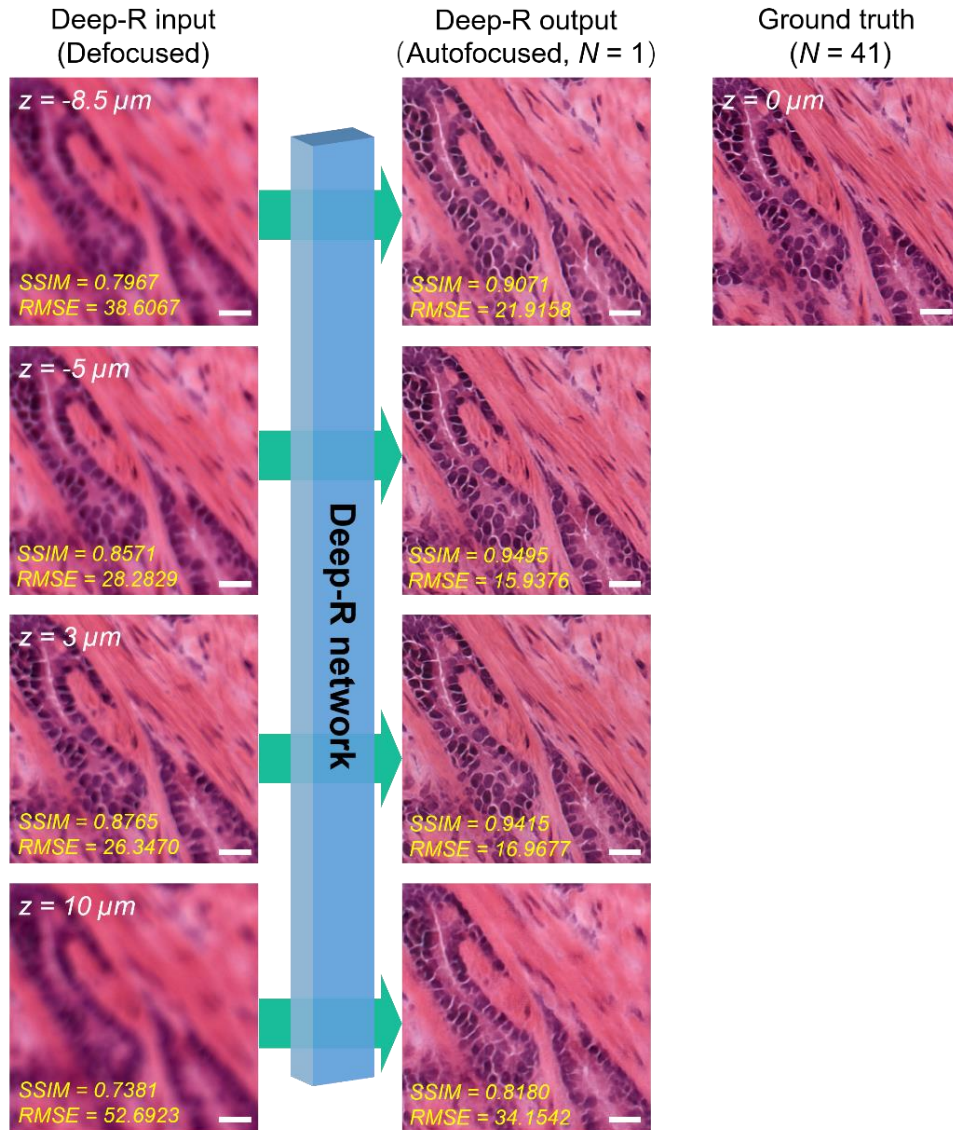


Fig. 7. Deep-R based autofocusing of brightfield microscopy images. The success of Deep-R is demonstrated by blindly autofocusing various defocused brightfield microscopy images of human prostate tissue sections. Scale bars, 20 μm .

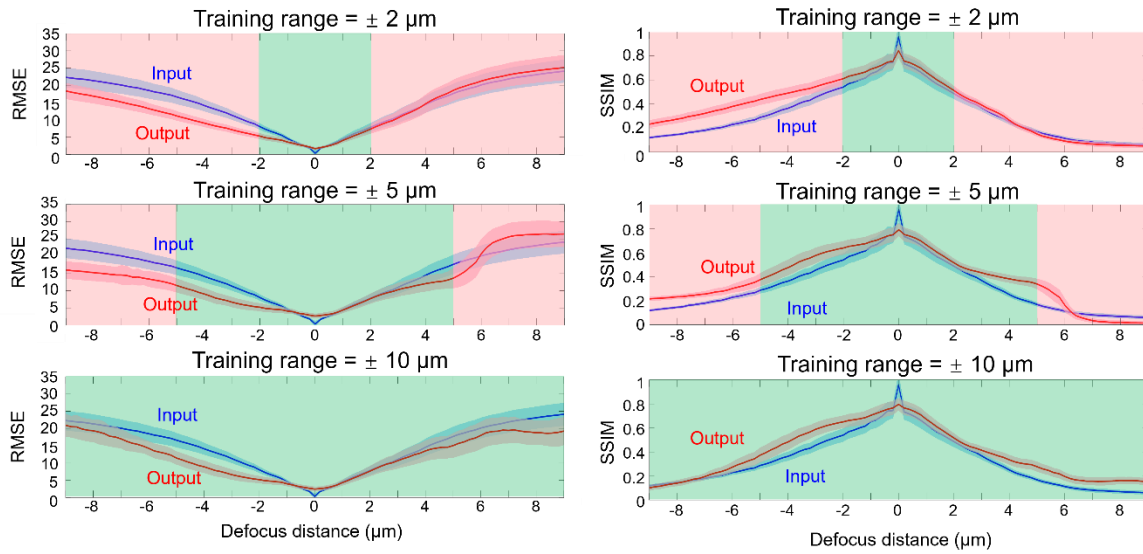


Fig. 8. Comparison of Deep-R autofocusing performance using different defocus training ranges.

Mean and standard deviation of (a) RMSE and (b) SSIM values of the input and output images at different defocus distances. Three different Deep-R networks are reported here, each trained with a different defocus range, spanning $\pm 2\mu\text{m}$, $\pm 5\mu\text{m}$, and $\pm 10\mu\text{m}$, respectively. The curves are calculated using 26 unique sample FOVs, each with 512×512 pixels.

Focusing criterion	Average time (sec/mm ²)	Standard deviation (sec/mm ²)
Vollath4³⁹	42.91	3.16
Vollath5³⁹	39.57	3.16
Standard deviation	37.22	3.07
Normalized variance¹⁰	36.50	0.36
Deep-R (CPU)	20.04	0.23
Deep-R (GPU)	2.98	0.08

Table. 1. Comparison of Deep-R computation time per 1 mm² of sample FOV (captured using a 20×/0.75NA objective lens) compared against other state-of-the-art autofocusing methods.